Proceedings of the Canadian Society for Mechanical Engineering International Congress 2022
CSME Congress 2022
June 5-8, 2022, Edmonton, AB, Canada

A GROUNDED AND TUNABLE MULTI-STABLE NONLINEAR ENERGY SINK: TRANSIENT RESPONSES

Haining Li[1], Kefu Liu[1], Jian Deng[2], Bing Li[3]
[1]Department of Mechanical Engineering, Lakehead University, Thunder Bay, Canada
[2]Department of Civil Engineering, Lakehead University, Thunder Bay, Canada
[3]College of Mechanical and Electrical Engineering, Harbin Institute of Technology, Shenzhen, China

Abstract—In this paper, a piezoelectric energy harvester with a grounded and tunable multi-stable nonlinear energy sink (NES) has been developed to achieve vibration suppression (VS) and energy harvesting (EH) simultaneously. The NES consists of a cantilever beam whose free end is attached by a small magnet and a movable holder containing two magnets. And the three magnets face a stationary magnet on the base whose height can be manually adjusted. The mono-stable NES (MNES), bi-stable NES (BNES) and tri-stable NES (TNES) can be achieved by moving the holder along the beam or raising or lowering the stationary magnet manually. The electromechanical model of the system is derived from the lumped parameter model, and the magnetic force model is deduced based on the magnetic dipole approach. Next, a series of simulations are conducted to investigate the VS and EH performance of the systems with the grounded MNES, BNES and TNES under the low and high-level impact excitation. The simulation results depict that the systems with the MNES and BNES will have a better performance in VS when the excitation level is low and high, respectively, and the system with the MNES outperforms in EH among the three systems for both low and high excitation levels.

Keywords-vibration energy harvesting; vibration suppression; multi-stable nonlinear energy sink; magnetic dipole approach;

I. INTRODUCTION

Vibration widely exists in machines and civil structures. Such ambient vibration may be caused by wind, operation of the machine or human activity. A vibration energy harvester (VEH) is a device that converts mechanical motion to electricity, which can solve the battery changing issue for the wireless sensor network.

A traditional VEH consists of a linear oscillator that operates in a narrow frequency bandwidth. In order to widen the bandwidth, various nonlinear VEHs have been proposed [1]. According to the system stability, the nonlinear VEHs can be classified as mono-stable and multi-stable such as bi-stable or tri-stable. A piezoelectric vibration energy harvester (PVEH) reported in [2] consists of a piezoelectric cantilever beam with a tip magnet subjected to an external magnetic field generated by a pair of fixed magnets. Such a mono-stable system can exhibit softening or hardening behaviors when the magnetic interaction is adjusted. By applying different external magnet tuning strategies, a bi-stable energy harvester (BEH) can be achieved. As shown in [3], the BEH can enhance the power output performance. Further, tri-stable energy harvesters (TEHs) have been proposed in order to reduce the depth of the BEH's potential wells. Based on the configuration of the BEH in [3], a TEH was achieved by tuning the angular orientations [4] or the spatial positions [5] of the fixed magnets. The studies showed that the optimally designed TEHs outperform the BEHs in terms of the voltage output.

On the other hand, vibration that exists in machines and civil structure is harmful, and it may cause resonance and even failure of the system. A vibration absorber is a device used to suppress the vibration of the primary system. A traditional linear vibration absorber mainly operates in the narrow frequency bandwidth. The nonlinear energy sink (NES) was proposed for the purpose of achieving wideband vibration suppression (VS). The NES consists of a small mass and essential nonlinear spring so that it can be weakly coupled with the primary system. The NES possesses some unique features such as target energy transfer (TET) and strongly modulate resonance (SMR) which can significantly enhance the vibration suppression performance. For the past two decades, various kinds of NES have been proposed by researchers, such as rotational NES [6], mono-stable NES (MNES) [7] and multi-stable NES such as bi-stable NES (BNES) [8, 9] and tri-stable NES (TNES) [10]. The study has shown that the multi-stable NES can achieve highly efficient TET in a wider band.

Since the 2-degree-of-freedom PVEH and NES share a similar structure, it is much desirable to achieve VS and energy harvesting (EH) simultaneously by a well-designed NES. An MNES based PVEH has been proposed in [11]. The apparatus possesses the characteristics of the 1:1 resonance TET and initial energy dependence. The study shows a significant VS effect and the broadband voltage output can also be achieved. The study reported in [12] proposed a PVEH with BNES. The VS and EH performance of the proposed PVEH is compared with that of a linear absorber under the impact excitation. Besides, a tuned BNES was proposed in [13] to further improve the VS and EH performances.

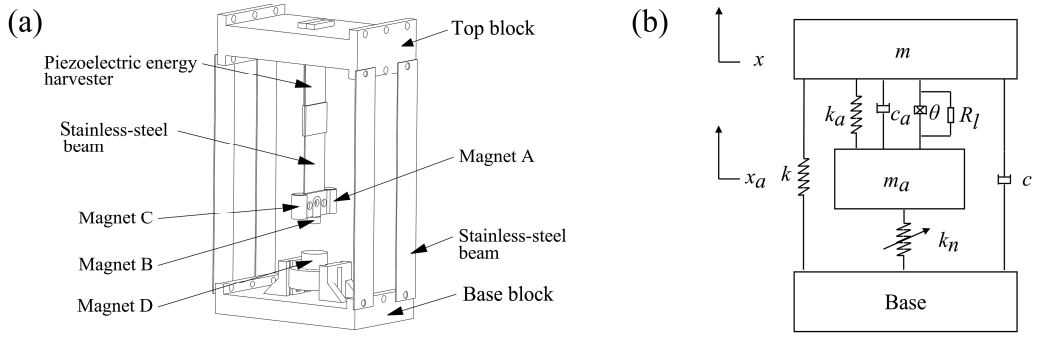

Figure 1. (a) 3D CAD drawing of a primary system attached by a tunable multi-stable NES, (b) lumped parameter model.

So far, the proposed MNESs and multi-stable NESs that can achieve VS and EH simultaneously are considered to be ungrounded as the nonlinear spring is connected between the NES mass and the primary mass. In this study, a grounded PVEH with a tunable multi-stable NES is proposed. The proposed NES consists of one stationary magnet and a cantilever beam whose free end is attached by a moveable assembly of two magnets and one tip magnet. By varying the gap between the stationary magnet and the tip magnet, and the distance between the magnet assembly and the tip magnet, the NES can assume three states: mono-stable, bi-stable or tri-stable. The rest of the paper is organized as follows: Section II presents the proposed apparatus, and derives the electromechanical model based on the lumped parameter model of the system, and then the magnetic force model is derived according to the magnetic dipole approach. Section III evaluates the performance under the transient responses by conducting the numerical simulation. Section IV draws the main conclusions of the study.

II. APPARATUS AND MODELLING

A. The apparatus and electromechanical model

Fig. 1(a) shows a CAD drawing of the apparatus developed for this study. The primary system consists of a top block and base block which are connected by four stainless-steel beams. The proposed tunable multi-stable NES comprises a cantilever beam attached with a tip magnet and a movable assembly of 2 magnets. The cantilever beam is composed of a unimorph piezoelectric transducer (S128-J1FR-1808YB, Midé Corporation) and a stainless-steel beam. One end of the cantilever beam is clamped to the top block while its other end is attached with a small cylindrical magnet B and a holder for two identical cylindrical magnets A and C. The holder for magnets A and C can slide along the beam. A large cylindrical magnet D is fixed in a holder that can slide vertically inside a stand fastened to the base block. When the primary beams and the cantilever beam are at their equilibrium position or undeflected, the four magnets situate on the same vertical plane and magnets B and D are colinear. By sliding the holder of magnet D, the distance between magnet B and magnet D can be adjusted. Fig. 1(b) shows the lumped parameter model of the proposed apparatus, where x and x_a represent the displacement of the primary mass and NES mass, respectively, the magnetic interaction is considered as a nonlinear spring with the nonlinear stiffness k_n. The equations governing the dynamics of the system can be represented by:

$$m\ddot{x} + c\dot{x} + kx - \left(c_a\dot{u} + k_a u + \theta v\right) = 0 \tag{1}$$

$$m_a\ddot{x}_a + \left(c_a\dot{u} + k_a u + \theta v\right) - f_n = 0 \tag{2}$$

$$c_p\dot{v} + \frac{v}{R_l} - \theta\dot{u} = 0 \tag{3}$$

where m, c, and k are the mass, damping coefficient and stiffness of the primary system, respectively; m_a, c_a and k_a is the mass, damping coefficient and stiffness of the NES system, respectively; θ is the electromechanical coupling coefficient of the PEH, f_n denotes the nonlinear magnetic force applied to the NES mass, R_l is the load resistance, c_p is the capacitance of the PEH, and $u = x_a - x$ represents the relative displacement between the primary mass and the NES mass.

B. Magnetic force model

Fig. 2 illustrates two symmetric situations of the deformed cantilever beam as the primary mass moves identically to the negative or the positive position on X-axis where O' represents the middle point of the fixed end of the cantilever beam. And the central axis of the cantilever beam will always be on plane XZ. The figure also depicts the spatial positions and polarities of the four magnets where $\boldsymbol{m}_A$, $\boldsymbol{m}_B$, $\boldsymbol{m}_C$, $\boldsymbol{m}_D$ are the magnetic moment vectors, A, B, C and D are the center positions of magnets, $\boldsymbol{r}_{DA}$ represents a vector from A to D, $\boldsymbol{r}_{DB}$ represents a vector from B to D, and vector $\boldsymbol{r}_{DA}$'s projection on the x-z plane is represented by $\boldsymbol{r}_{DAxz}$. Note that the direction of $\boldsymbol{m}_B$ is opposite to that of $\boldsymbol{m}_A$, $\boldsymbol{m}_C$ and $\boldsymbol{m}_D$.

The total nonlinear magnetic force f_n in the x-direction consists of an attractive magnetic force f_{DBx} between magnet D and magnet B, and two repulsive magnetic forces: f_{DAx} between magnet D and magnet A and f_{DCx} between magnet D and magnet C. Since magnets A and C are identical and symmetrical about the central line of the beam, the values of f_{DAx} and f_{DCx} are equal. Then the total nonlinear magnetic force can be expressed as:

$$f_n = f_{DBx} + f_{DAx} + f_{DCx} = f_{DBx} + 2f_{DAx}. \tag{4}$$

Fig. 3(a) shows the side view of Fig. 2 when the cantilever beam is undeformed, where d is the vertical distance between

magnet D and magnet B, h is the gap between the center of magnet A or C and the center of magnet B, l is the length of the cantilever beam, and w is the distance between the axis of magnet B and that of magnet A or C. Fig. 2(b) shows the front view of Fig. 2 when the cantilever beam is deformed to the right side and the primary mass's displacement x is positive, where α is the angle between $\boldsymbol{m}_B$ and $\boldsymbol{m}_D$, and β is the supplement of the angle between $\boldsymbol{m}_D$ and $\boldsymbol{r}_{DB}$, x and z are the transverse and longitudinal displacements of the center of magnet B, respectively.

In this paper, the magnetic dipole approach [14] is used to determine the magnetic force between two magnets. Firstly, the magnetic force between magnet D and magnet B is considered. According to the dipole assumption, the force exerted by magnet D on magnet B is given by:

$$\boldsymbol{f}_{DB} = \nabla\left(\boldsymbol{B}_{DB} \cdot \boldsymbol{m}_B\right) \tag{5}$$

where $\boldsymbol{B}_{DB}$ is the magnetic flux density generated by magnet D upon B. Equation (5) can be expanded as:

$$\begin{aligned}\boldsymbol{f}_{DB} = \frac{3\mu_0 m_D m_B}{4\pi r_{DB}^4}\Big[&\hat{\boldsymbol{r}}_{DB}\left(\hat{\boldsymbol{m}}_B \cdot \hat{\boldsymbol{m}}_D\right) - 5\hat{\boldsymbol{r}}_{DB}\left(\hat{\boldsymbol{m}}_D \cdot \hat{\boldsymbol{r}}_{DB}\right)\left(\hat{\boldsymbol{r}}_{DB} \cdot \hat{\boldsymbol{m}}_B\right) \\ &+ \hat{\boldsymbol{m}}_B\left(\hat{\boldsymbol{m}}_D \cdot \hat{\boldsymbol{r}}_{DB}\right) + \hat{\boldsymbol{m}}_D\left(\hat{\boldsymbol{m}}_B \cdot \hat{\boldsymbol{r}}_{DB}\right)\Big]\end{aligned} \tag{6}$$

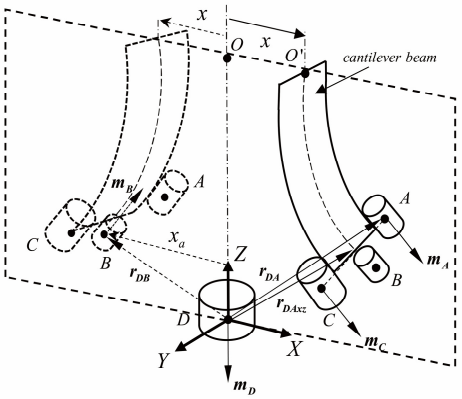

Figure 2. Spatial positions of the magnets.

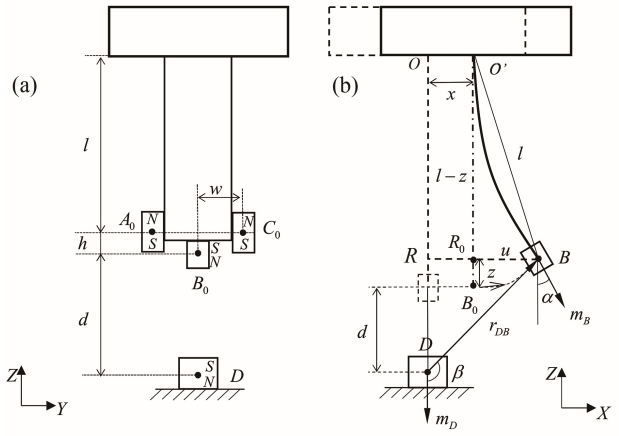

Figure 3. (a) Side view and (b) front view of the apparatus.

where m_B, m_D, and r_{BD} are the magnitude of $\boldsymbol{m}_B$, $\boldsymbol{m}_D$, and $\boldsymbol{r}_{DB}$, respectively; $\hat{\boldsymbol{m}}_B$, $\hat{\boldsymbol{m}}_D$, and $\hat{\boldsymbol{r}}_{BD}$ are the unit vector of $\boldsymbol{m}_B$, $\boldsymbol{m}_D$, and $\boldsymbol{r}_{DB}$, respectively. These unit vectors can be expressed as:

$$\begin{aligned}&\hat{\boldsymbol{m}}_B = \left[\sin(\alpha)\ -\cos(\beta)\ 0\right],\ \hat{\boldsymbol{m}}_D = \left[0\ -1\ 0\right], \\ &\hat{\boldsymbol{r}}_{DB} = \left[-\sin(\beta)\ \cos(\beta)\ 0\right].\end{aligned} \tag{7}$$

Substituting the above unit vectors in the dot products of (6) and the magnetic force in the x-direction can be obtained in the following form:

$$\begin{aligned}f_{DBx} = -\frac{3\mu_0 m_D m_B}{4\pi r_{BD}^4}\Big\{&\sin(\beta)\left[\cos(\alpha) - 5\cos(\beta)\cos(\beta-\alpha)\right] \\ &+ \sin(\alpha)\cos(\beta)\Big\}.\end{aligned} \tag{8}$$

Since the slope of the beam's tip is relatively small, it is assumed that $\angle BOB_0 \approx \alpha$. Also, it is noted that β can be found from the triangle DRB in Fig. 3(b). The trigonometric relationship in (8) can be expressed as follows:

$$\sin(\alpha) = \frac{u}{l};\ \cos(\alpha) = \frac{l-z}{l}; \tag{9}$$

$$\sin(\beta) = \frac{x_a}{r_{DB}};\ \cos(\beta) = -\frac{z+d}{r_{DB}}; \tag{10}$$

$$\begin{aligned}\cos(\beta-\alpha) &= \cos(\alpha)\cos(\beta) + \sin(\alpha)\sin(\beta) \\ &= \frac{l-z}{l}\left(-\frac{z+d}{r_{DB}}\right) + \frac{x_a}{r_{DB}}\frac{x_a}{l} \\ &= \frac{x_a^2 - lz - ld + zd + z^2}{l r_{DB}}.\end{aligned} \tag{11}$$

where $z = l - \sqrt{l^2 - u^2}$. Substituting the above expressions into (8) yields

$$\begin{aligned}f_{DBx} = -\frac{3\mu_0 m_D m_B}{4\pi r_{DB}^5 l}\Big\{&x_a(l-z) - u(d+z) \\ &-\frac{5}{r_{DB}^2}\left[-z^3 + (l-2d)z^2 + (2dl - ux_a - d^2)z + d^2 l - ux_a d\right]\Big\}\end{aligned} \tag{12}$$

Similarly, the magnetic force between magnet A and magnet D in the x-direction can be found as:

$$\begin{aligned}f_{DAx} = \frac{3\mu_0 m_D m_A}{4\pi r_{DA}^4 l}\Big\{&\frac{x_a(l-z) - u(d+z)}{r_{DAxz}} - \frac{5}{r_{DAxz}^3}\left[-z^3 + (l-2d_0)z^2\right. \\ &\left.+ (2d_0 l - ux_a - d_0^2)z + d_0^2 l - ux_a d\right]\Big\}\end{aligned} \tag{13}$$

where $d_0 = d + h$. Substituting (12) and (13) into (4), then the nonlinear magnetic force model can be obtained. All the parameters' values are listed in Table I. Note that the amplitudes of the magnetic moment vectors for magnets A, B, C and D are obtained by an experimental identification given in [15]. For the sake of comparison, three configurations of the NESs are considered in this study: MNES d=0.0487 m, h=0.0187 m; BNES d=0.0467 m, h=0.0157 m; TNES d=0.0367 m, h=0.0197 m.

TABLE I. PARAMETERS VALUE OF THE APPARATUS

symbol	Parameters	
	Parameter name	***value***
μ_0	Vacuum permeability	$4\pi\times10^{-7}$
m_A, m_C	Magnitudes of magnetic moment vector of magnet A and C (H.m/T)	4.30
m_B	Magnitude of magnetic moment vector of magnet B (H.m/T)	0.83
m_D	Magnitude of magnetic moment vector of magnet D (H.m/T)	18.00
w	Distance between the axis of magnet B and magnet A or C (m)	0.025
k_a	Stiffness of the cantilever beam (N/m)	47.39
l	Length of the cantilever beam (m)	0.12
k	Stiffness of the primary system (N/m)	189
m	Mass of the primary system(kg)	0.44
m_a	Mass of the NES (kg)	0.066
c	Damping coefficient of the primary system (Ns/m)	0.125
c_a	Daping coefficient of the NES (Ns/m)	0.067
θ	Electromechanical coupling coefficient of the piezoelectric transducer (N/V)	1.88×10^{-4}
R_l	Load resistance (ohm)	5×10^{6}

C. *The potential energy of the system*

The potential energy of the NES can be obtained by taking the integral of the total restoring force of the NES f_a which can be expressed as follows:

$$f_a = k_a\left(x_a - x\right) - f_n \tag{14}$$

Note that the total restoring force is related to three factors: the displacement of the primary system x; the displacement of the NES x_a; and the magnetic force f_n. In other words, the position of the primary system will affect the potential energy of the NES. Figs. 4(a) (b) and (c) show the potential energy verse x_a of the MNES, BNES and TNES for three different values of x. It can be observed that the NESs are in symmetrical mono-stable, bi-stable and tri-stable stability states when x=0, and they become asymmetric mono-stable, bi-stable and tri-stable systems as the absolute value of x increases to 0.003 m. It should be mentioned that Fig. 4 only shows the local potential of the grounded NESs. It cannot tell where the NESs will finally rest according to the local potentials. To get the global potentials of the grounded NES systems, the equilibrium positions of the primary systems that they are attached to need to be considered. The primary systems with the grounded MNES, BNES and TNES will have multiple equilibrium positions due to the changing elastic forces induced by the NESs. And the equilibrium position of the primary system x_e fulfills the following condition:

$$kx_e = k_a(x_{ae} - x_e) \tag{15}$$

where x_{ae} is the equilibrium position of the NES. Accordingly, the global potential of the grounded NESs can be determined, which can tell the positions that the primary system and the NES will finally rest.

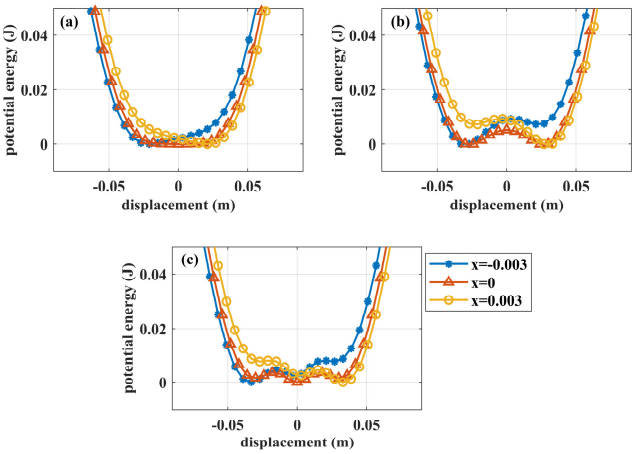

Figure 4. The potential energy of the different NESs verse x_a when varying x: (a) MNES; (b) BNES; (c)TNES.

III. NUMERICAL SIMULATION

A. *Transient response*

To compare the VS and EH performance of the system with the MNES BNES and TNES, a series of simulations to get their transient responses is conducted. In the simulation, the impulsive force $f_p(t)$ which is applied to the primary system is a half-sine signal with amplitude A and period T:

$$f_p(t) = \begin{cases} A\sin\left(\dfrac{2\pi t}{T}\right), & 0<t<\dfrac{T}{2} \\ 0, & t \ge \dfrac{T}{2} \end{cases} \tag{16}$$

where the period T=0.3 s . Two initial energy levels are considered in the simulations: the low initial energy level (A=1.2 N) and high initial energy level (A=8 N). In this case, the electromechanical equations of the system (1)-(3) can be rewritten as follows:

$$m\ddot{x} + c\dot{x} + kx - \left(c_a\dot{u} + k_a u + \theta v\right) = f_p(t) \tag{17}$$

$$m_a\ddot{x}_a + \left(c_a\dot{u} + k_a u + \theta v\right) - f_n = 0 \tag{18}$$

$$c_p\dot{v} + \frac{v}{R_l} - \theta\dot{u} = 0. \tag{19}$$

The values of the parameters in the above equations are listed in Table I. By solving (17)-(19) with the zero initial condition for the system with the TNES, and the initial conditions of (x, $\dot{x}$, x_a, $\dot{x}_a$, v)=(0.003, 0, 0.022, 0, 0) and (0.004, 0, 0.031, 0, 0) for the systems with the MNES and BNES, respectively, in the period of 20 s using the MATLAB ODE45 solver, the transient responses of the primary system, NES and load voltage can be obtained. Besides, the EH performance is evaluated by the accumulated energy in NES E, which is defined as follows:

$$E(t) = \int_0^t \frac{v(t)^2}{R_l}dt \tag{20}$$

where t is the duration of the simulation, v is the load voltage and R_l represents the resistance of the load resistor.

B. Results and discussion

1) Low initial energy level

When the amplitude of the impulsive force A=1.2 N, the time responses of the displacements of the primary systems with locked NES, MNES, BNES and TNES, and the displacements of the MNES, BNES and TNES are shown in Fig. 5. Note that to conduct the simulation of the system with a locked NES is by solving (17) with the primary mass equal to $m+m_a$, and setting u and v to zero. Fig. 5 shows that the MNES performs the snap-through motion between its equilibrium positions initially, and it dissipates the impulse energy rapidly within 11.8 s to decrease the initial amplitude of the primary system to 4%. By contrast, it takes 13.24 s and 19.5 s for the systems with the BNES and TNES to dissipate the initial amplitude to 4%. And it also can be seen that the BNES and TNES are only oscillating in one of their potential wells.

Figs. 6(a)-(c) show the wavelet transform (WT) spectra of the displacements of the primary systems with the MNES, BNES and TNES, and the WT spectra of the displacements for their corresponding NESs are shown in Figs. 6(d)-(f). It can be seen in Figs. 6(a) and (d) that the 1:1 internal resonance occurs between the MNES and the primary system when the MNES performs the snap-through motion at the first 1.5 s. As shown in Figs. 6(b) and (e), although the 1:1 resonance phenomenon occurs in the system with the BNES initially. However, the nonlinearity does not activate due to the BNES only oscillating in the single stability potential well. Figs. 6(c) and (f) show the primary system and TNES oscillates at their own natural frequencies, which means the TET does not occur.

Fig. 7 shows the accumulated energy for systems with different NESs under the low-level impact excitation. It shows that the system with the MNES is the most efficient in EH. Due to MNES performing the snap-through movement at the beginning, the accumulated energy of MNES shows a rapid rise initially and then stops at 0.52 mJ. By contrast, the systems with BNES and TNES are far less efficient in EH with merely 0.06mJ and 0.04mJ total accumulated energy, respectively.

2) High initial energy level

For the case of the system under the high-level impact excitation, The time responses of the displacements of the primary systems with the locked NES, MNES, BNES and TNES, and the displacements of the corresponding NESs are shown in Fig. 8. As shown the system with the MNES, BNES and TNES perform the snap-through motion initially and then rest in one of their equilibrium positions. The VS effect can be clearly observed from the transient responses of the three systems. It takes 14.04 s, 9.55 s and 13.58 s to decrease the initial amplitude to 4% for systems with the MNES, BNES and TNES, respectively. Thus, the system with the BNES is the most efficient in VS among the three systems.

Figs. 9(a)-(c) show the WT spectra of the displacements of the primary systems with the MNES, BNES and TNES, and the WT spectra of the displacements of their corresponding NESs are shown in Figs. 9(d)-(f). It can be observed in Fig. 9 that the 1:1 resonance has been triggered and the TET has been established between the primary systems and NESs of the three systems. Taking the system with the BNES for example, it can be seen in Figs. 9(b) and (e) that the dominant frequencies of the primary system and BNES are located around their natural frequencies, which indicates the TET occur. And such a phenomenon can also be observed in the other two systems.

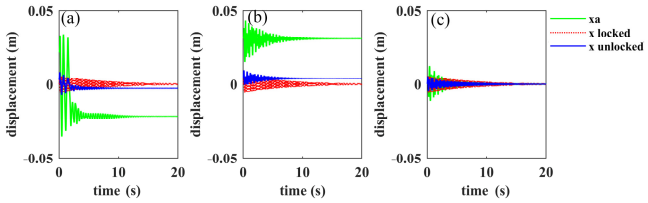

Figure 5. Transient responses of the systems with four different NESs when A=1.2 N, red dash line and blue solid for the displacement of primary mass with locked and unlocked NES, green solid line for the NES's displacement: (a) MNES; (b) BNES; (c) TNES.

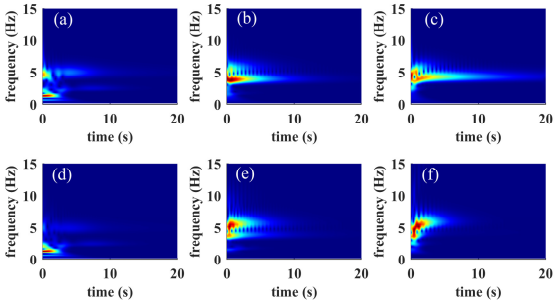

Figure 6. WT spectra of the transient responses of the systems with four different NESs when A=1.2 N, upper plots for the primary displacements and lower plots for the NES displacements: (a)(d) MNES; (b)(e) BNES; (c)(f) TNES.

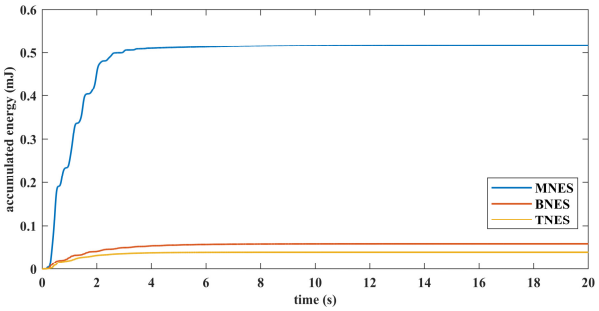

Figure 7. Accumulated energy of the systems with different NESs when A=1.2 N.

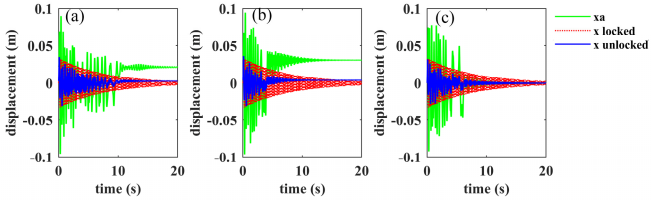

Figure 8. Transient responses of the systems with four different NESs when A=8 N, red dash line and blue solid for the displacement of primary mass with locked and unlocked NES, green solid line for the NES's displacement: (a) MNES; (b) BNES; (c) TNES.

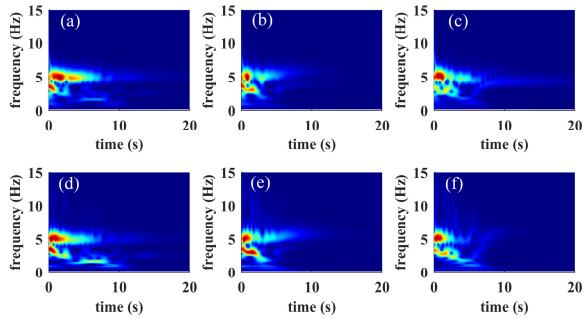

Figure 9. WT spectra of the transient responses of the systems with four different NESs when A=8 N, upper plots for the primary systems' displacements and lower plots for the NESs' displacements: (a)(d) MNES; (b)(e) BNES; (c)(f) TNES.

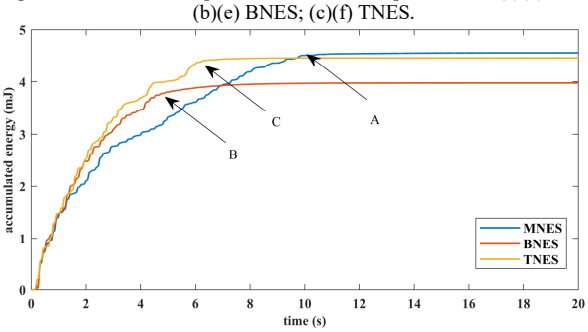

Figure 10. Accumulated energy of the systems with different NESs when A=8 N.

Fig. 10 shows the accumulated energy for the systems with different NESs under the high-level impact excitation. It depicts that the system with the MNES is the most efficient in EH with 4.55 mJ of total accumulating energy. And the total accumulated energy for the systems with the BNES and TNES is 3.97 mJ and 4.45 mJ, respectively. The arrows A, B and C in Fig. 10 point out the end of the rapid increase period of the accumulated energy, which is at 10.37 s, 4.52 s and 6.06 s for the systems with the MNES, BNES and TNES, respectively. It can be found that the system with the TNES has better EH performance than the systems with the BNES and MNES at the first 9 s since it has larger separation distances between its two side potential wells. After that, the system with the MNES outperforms in EH since it lasts longer to perform in the snap-through movement.

IV. Conclusions

In this study, a PVEH with a grounded multi-stable NES has been developed. The NES can be manually tuned to achieve three different stability states referred to as MNES, BNES, and TNES, respectively. The electromechanical model of the system is derived from the lumped parameter model, and the magnetic force model is established based on the magnetic dipole approach. The simulation is conducted to investigate the VS and EH performances of the systems with MNES, BNES and TNES under the low and high-level impact excitation. The results depict that under the low-level impact excitation, the system with the MNES has the lowest energy threshold to engage the high-efficiency TET. Thus, it outperforms in VS among the three systems, and it also has a better performance in EH due to its low energy threshold to operate in the snap-through oscillation. When the initial energy level is high enough, the MNES, BNES and TNES can both perform the snap-through motion initially. In this case, the system with the BNES has better VS performance among the three systems. On the other hand, the systems with the BNES and TNES perform better in EH initially since they have larger separation distances between their two side potential wells. However, the system with the MNES can harvest more energy eventually because it lasts longer to perform the snap-through motion.

References

[1] Z. Yang, S. Zhou, J. Zu, and D. Inman, "High-Performance Piezoelectric Energy Harvesters and Their Applications," *Joule,* vol. 2, no. 4, pp. 642-697, 2018.

[2] S. C. Stanton, C. C. McGehee, and B. P. Mann, "Reversible hysteresis for broadband magnetopiezoelastic energy harvesting," *Applied Physics Letters,* vol. 95, no. 17, 2009.

[3] A. Erturk, J. Hoffmann, and D. J. Inman, "A piezomagnetoelastic structure for broadband vibration energy harvesting," *Applied Physics Letters,* vol. 94, no. 25, 2009.

[4] J. Cao, S. Zhou, W. Wang, and J. Lin, "Influence of potential well depth on nonlinear tristable energy harvesting," *Applied Physics Letters,* vol. 106, no. 17, pp. 173903, 2015.

[5] L. Haitao, Q. Weiyang, L. Chunbo, D. Wangzheng, and Z. Zhiyong, "Dynamics and coherence resonance of tri-stable energy harvesting system," *Smart Materials and Structures,* vol. 25, no. 1, pp. 015001, 2016.

[6] A. S. Saeed, M. A. Al-Shudeifat, and A. F. Vakakis, "Rotary-oscillatory nonlinear energy sink of robust performance," *International Journal of Non-Linear Mechanics,* vol. 117, 2019.

[7] Z. Zhang, Z.-Q. Lu, H. Ding, and L.-Q. Chen, "An inertial nonlinear energy sink," *Journal of Sound and Vibration,* vol. 450, pp. 199-213, 2019/06/23/, 2019.

[8] G. Habib, and F. Romeo, "The tuned bistable nonlinear energy sink," *Nonlinear Dynamics,* vol. 89, no. 1, pp. 179-196, 2017.

[9] D. Qiu, T. Li, S. Seguy, and M. Paredes, "Efficient targeted energy transfer of bistable nonlinear energy sink: application to optimal design," *Nonlinear Dynamics,* vol. 92, no. 2, pp. 443-461, 2018.

[10] H. Yao, Y. Cao, Y. Wang, and B. Wen, "A tri-stable nonlinear energy sink with piecewise stiffness," *Journal of Sound and Vibration,* vol. 463, 2019.

[11] Y. Zhang, L. Tang, and K. Liu, "Piezoelectric energy harvesting with a nonlinear energy sink," *Journal of Intelligent Material Systems and Structures,* vol. 28, no. 3, pp. 307-322, 2016.

[12] M. Rezaei, R. Talebitooti, and W.-H. Liao, "Exploiting bi-stable magneto-piezoelastic absorber for simultaneous energy harvesting and vibration mitigation," *International Journal of Mechanical Sciences,* vol. 207, pp. 106618, 2021/10/01/, 2021.

[13] S. Fang, K. Chen, J. Xing, S. Zhou, and W.-H. Liao, "Tuned bistable nonlinear energy sink for simultaneously improved vibration suppression and energy harvesting," *International Journal of Mechanical Sciences,* vol. 212, 2021.

[14] K. W. Yung, P. B. Landecker, and D. D. Villani, "An analytic solution for the force between two magnetic dipoles," *Physical Separation in Science and Engineering,* vol. 9, no. 1, pp. 39-52, 1998.

[15] H. li, "A tunable multi-stable piezoelectric vibration energy harvester," unpublished.